Aeroacoustics Conferences
20-23 May 2019, Delft, The Netherlands
25th AIAA/CEAS Aeroacoustics Conference
10.2514/6.2019-2574

A new MEMS microphone array for the wavenumber analysis of wall-pressure fluctuations: application to the modal investigation of a ducted low-Mach number stage

Édouard Salze[a], Emmanuel Jondeau[b], Antonio Pereira[c], Simon L. Prigent[d] and Christophe Bailly[e]
Univ Lyon, École Centrale de Lyon and LMFA UMR CNRS 5509, Écully, France, F-69134

The modal analysis of modern turbofan engines encounters several limitations, amongst which lies the difficulty to position several microphones on a realistic test-rig. Another difficulty is the managment of a high number of unsteady measurement channels. Interest is growing around digital MEMS microphones, which do not require a front-end acquisition system and allow the deployment of large arrays of sensors. This study is focused on the design of a new microphone array using digital MEMS microphones. The associated signal processing in the wavenumber domain involves a spatial Fourier transform of the pressure. This representation allows a quantitative and explicit extraction of the acoustic component of wall-pressure fluctuations, and thus provides an efficient way for in-flow acoustic measurements. The array is tested and validated in acoustic and hydrodynamic academic configurations. The feasibility of a modal analysis of a low-Mach number turbofan stage is then demonstrated.

I. Introduction

Modal analysis has become a common tool for the experimental characterization of ducted turbofan engines[3, 8]. It enables the fine analysis of new engine architectures, such as ultra-high bypass ratios, or heterogeneous guide vanes[12]. In this context, the experimental campaigns are usually conducted using arrays of tens of microphones, flush-mounted inside the duct. The implementation and the use of such microphone arrays in realistic engines or test rigs may raise several difficulties. The limited amount of space available on realistic engines – because of all the auxilliary systems required to operate the test – or the cost of unsteady high-frequency measurement channels may limit the number of microphones on the engine. A solution is the use of a large number of digital MEMS microphones mounted on printed circuit boards, which do not require a front-end acquisition system, and offer very small dimensions of a few millimeters.

Another difficulty lies in the characteristics of the measured wall-pressure fluctuations. The large dynamic range between the acoustic pressure of interest and the aerodynamic pressure associated with wall-bounded turbulence requires a separation between those two components. When the purpose is to keep only the acoustic contribution, this separation is also called *denoising*. It involves the reconstruction of the diagonal of the cross-spectral matrix, which is assumed to carry alone the energy of the aerodynamic wall-pressure fluctuations. When the purpose is also the study of the wall-bounded turbulence contribution, a direct measurement of the wall-pressure contribution is thus desirable.

In previous studies by some of the present authors [2, 13, 16], both aerodynamic and acoustic parts of the wall-pressure wavevector-frequency spectrum were obtained through original post-processing involving a spatial Fourier transform in polar coordinates. Results have been reported for measurements beneath a turbulent boundary layer, and the feasibility of obtaining pressure spectra by this original approach was demonstrated. Following these studies, a recent development was published in the context of automotive interior noise [5]. In the present work, a new microphone array with digital MEMS microphones is designed for the wavenumber analysis, validated in realistic experimental conditions, and then used for the modal analysis of a low-Mach number stage.

The paper is organized as follows. First, a new microphone array is carefully designed and manufactured. It

[a]Research Engineer at CNRS, edouard.salze@ec-lyon.fr
[b]Engineer at CNRS
[c]Research Engineer at École Centrale de Lyon
[d]Post-doctoral fellow at École Centrale de Lyon
[e]Professor at École Centrale de Lyon, AIAA senior member

enables the direct measurement of both acoustic and aerodynamic contributions to wall-pressure fluctuations. Then, the wavenumber approach is detailed and validated through two academic configurations: the first with an acoustic source, and the second in a wind tunnel designed for flow-acoustic measurements. Finally, direct measurements of wavenumber-frequency spectra are performed inside a low-Mach number turbofan stage to enable the modal analysis of the pressure field, and the analysis of the aerodynamic contributions at the same time.

II. Design and implementation of the MEMS array

A. System architecture

The final application – the modal analysis of a turbofan engine – requires a small-sized microphone, whose bandwidth covers the audio frequencies up to 20 kHz. In the literature, the use of quarter inch capacitive analog microphones is quite common [3, 8, 12]. That type of microphone offers a very high dynamics up to 160 dB or more, together with an extended bandwidth of 80 kHz or more. This type of microphone is indeed a good choice for laboratory applications. However, the diameter of such microphones – about 7 mm – is too big to allow the analysis of the turbulent wall-pressure, whose typical wavelengths are notably smaller. In addition, the length of the microphone's body is too big – around 40 mm long – to be installed in confined spaces such as stator vanes or interstage regions in turbofan engines. A good choice is the use of remote microphone probes, but the mechanical integration of such probes on realistic test-rigs might be difficult.

In the present study, the authors choose to implement INMP621 digital microphones, commercialized by InvenSense. That microphone has small dimensions – $4{\times}3{\times}1$ mm^3 –, and does not require any front-end acquisition set-up, thanks to its digital output. Furthermore, the reduced cost of such a sensor enables the implementation of arrays with a huge number of microphones. For the present study, a number of 32 microphones is implemented.

The MEMS array is operated using a 64 bits parallel 18 channels digital bus, synchronized at a frequency of 3.2 MHz (see Fig. 1). In this architecture, the first two channels are dedicated to clocks, and the 16 other channels are stereo channels used for the transfer of the 32 microphone signals. The clock signals are generated using an FPGA circuit, and the digital bus of microphone data is read in real time using the same FPGA circuit.

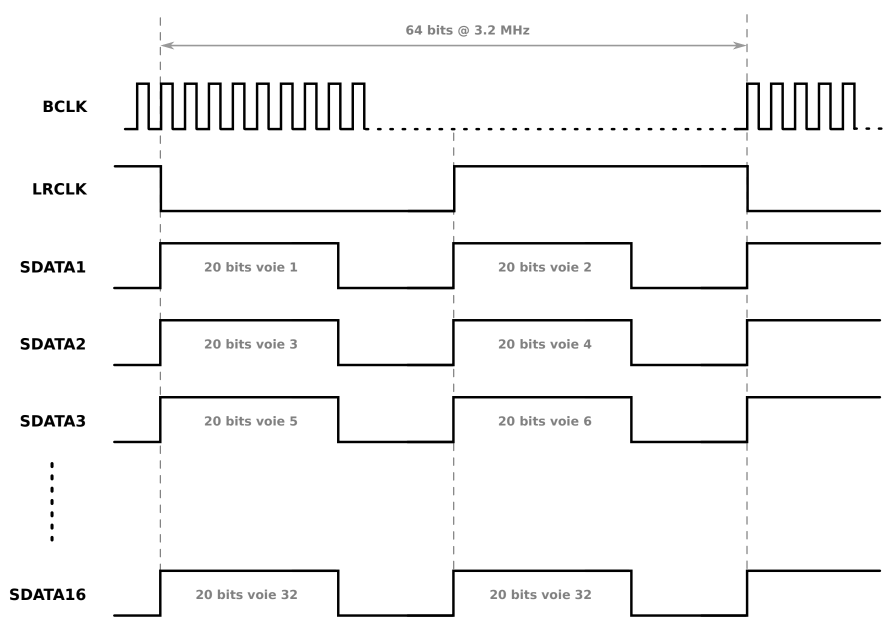

Fig. 1 Digital bus of the MEMS array.

The overall structure of the MEMS array is sketched in figure 2. The 32 microphones are mounted on a printed circuit board, and connected to the FPGA circuit. The FPGA circuit is the key element of the whole acquisition system:

it drives the digital intputs / outputs, generates the clock signals, reads the microphone data in real time, decodes the digital data. The FPGA circuit also drives the data exchange between the onboard memories and the RAM of the computer using Direct Memory Access protocoles (see Fig. 2). In the present study, a National Instrument 7820-R digital I/O card, with an FPGA circuit and inboard memory, has been chosen and programmed for those tasks.

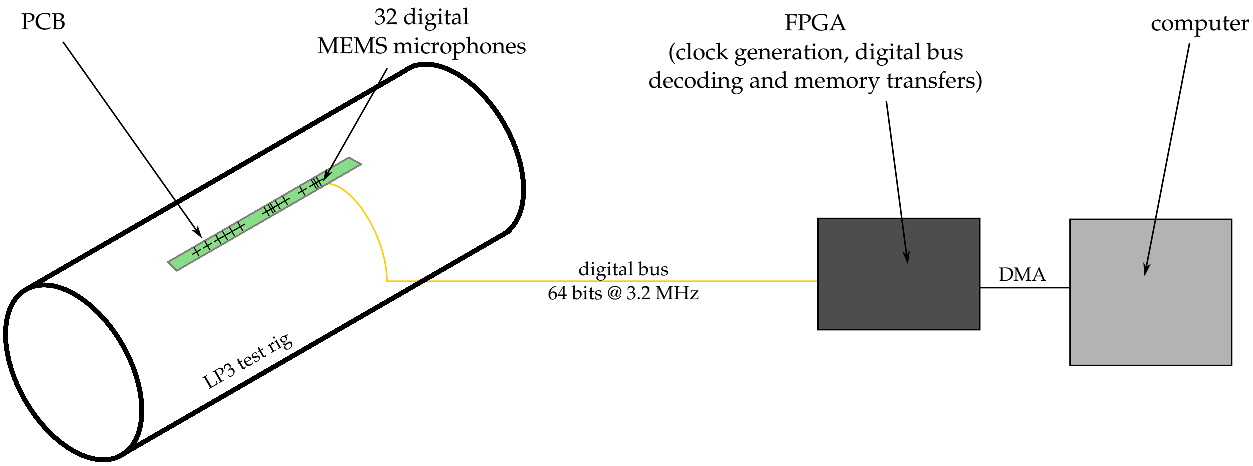

Fig. 2 Architecture of the digital acquisition system. Digital MEMS microphones are mounted on a printed circuit board. An FPGA circuit drives the digital bus and the data exchange with the computer.

B. Design of the microphone array

The 32 microphones MEMS array has a spatial extent of $L_1 = 40$ cm. This value allows the extraction of coherence functions of the acoustic pressure down to 500 Hz approximately. The smallest microphone separations are as small as possible, so as to enable the analysis of the highest wavenumbers in the pressure field – namely, the convected turbulence. Also, the separations between two neighbouring sensors are not uniform to present the best antenna response with the minimum sidelobes and reduced spatial aliasing. The optimized geometry of the array is plotted in figure 3. Note that, in that configuration, the left side of the antenna is different from the right side, and every distance between two microphones is unique. With 32 microphones, the co-array contains 488 elements on which the signal processing is performed.

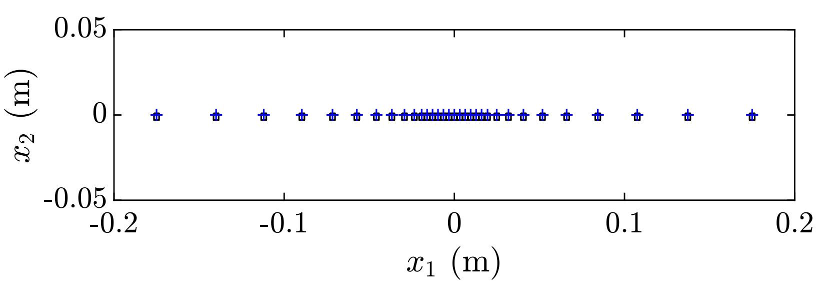

Fig. 3 Optimized geometry of the MEMS array.

III. Wavenumber approach and test-cases

A. Signal processing

The principle of a linear array of 32 flush-mounted microphones has been retained for this study. Unsteady pressure signals are simultaneously recorded over the 32 microphones at a sampling frequency of 50 kHz during a time period of 120 s. The Fourier transform $\hat{p}(\boldsymbol{k},\omega)$ of the pressure field $p(\boldsymbol{x},t)$ in space and in time is defined by

$$p(\boldsymbol{x},t) = \iint \hat{p}(\boldsymbol{k},\omega) e^{i(\boldsymbol{k}\cdot\boldsymbol{x}-\omega t)} d\boldsymbol{k}\, d\omega = \mathcal{F}^{-1}\left\{\hat{p}(\boldsymbol{k},\omega)\right\}$$

Assuming stationary random signals and ergodicity, the cross spectral matrix is defined as:

$$S_{ij}(\boldsymbol{x},\boldsymbol{\xi},\omega) = \lim_{T\to\infty} \frac{2\pi}{T} E\left[\hat{p}(\boldsymbol{x},\omega)\hat{p}^{\star}(\boldsymbol{x}+\boldsymbol{\xi},\omega)\right]$$

where $\boldsymbol{\xi} = (\xi_1, \xi_2)$ is the separation vector between two microphones located at $\boldsymbol{x}$ and $\boldsymbol{x}+\boldsymbol{\xi}$, and recall that the diagonal S_{ii} contains the power spectral densities of the array. The cross-spectra S_{ij} are extracted from time signals using 480 blocks of duration $T = 250$ ms with a 50% overlap between the blocks, using a Hann windowing. In practice, the wall-pressure field is assumed to exhibit homogeneous properties over the microphone array, that is $S_{ij}(\boldsymbol{x},\boldsymbol{\xi},\omega) = S_{ij}(\boldsymbol{\xi},\omega)$. The coherence γ is then defined from the cross-spectral quantities as

$$\gamma(\boldsymbol{\xi},\omega) = \sqrt{\frac{|S_{ij}(\boldsymbol{\xi},\omega)|^2}{S_{ii}(\omega)S_{jj}(\omega)}}$$

The one-dimensionnal streamwise wavenumber-frequency spectrum is directly computed by discretizing the following Fourier integral:

$$\Phi_{pp}(k_1,\omega) = \frac{1}{(2\pi)} \int S_{ij}(\xi_1,\omega) e^{-ik_1\xi_1} d\xi_1$$

where k_1 is the streamwise wavenumber.

At a given frequency f_0, the wavenumber spectrum is characterized by two contributions [1, 4, 6, 7]: an acoustic contribution around $k_0 = \omega/c_0$, and an hydrodynamic contribution due to the convection of wall-bounded turbulence, located around $k_c = \omega/U_c$.

θ is the angle between an impinging acoustic wavevector and the microphone array (see Fig. 4 at left). Such a plane wave will produce a spot on the wavenumber-frequency spectra, located at the frequency f and at the wavenumber $k_1 = k_0\cos\theta$, along the array direction (see Fig 4 at right). Positive wavenumbers correspond to waves propagating in the direction of the array, and negative wavenumbers correspond to waves propagating in the other direction. Limiting cases $k_1 = \pm k_0$ correspond to acoustic waves propagating in the exact direction of the antenna. The case $k_1 = 0$ corresponds to a wave impacting the array in the normal direction (see Fig. 4 at left).

The wavenumber representation of the pressure enables a spatial filtering. For instance, it is possible to integrate the positive wavenumbers, with a view to extract all contributions propagating from the left to the right. It is also possible to extract all contributions from the acoustic region :

$$S_{\mathrm{ii}}^{\mathrm{ac}}(\omega) = \int_{-(k0+\Delta k/2)}^{k0+\Delta k/2} \Phi_{pp}(k_1,\omega)\mathrm{d}k_1 \tag{1}$$

In this example, the spatial filtering enables the direct extraction of the acoustic spectrum apart from the hydrodynamic pressure, without any assumption on the pressure field. The spectral broadening, due to the limited spatial extent of the windows, is accounted for by adding the wavenumber resolution Δk in the integration limits of Eq. 1.

B. Acoustic test case

The MEMS array is aligned with a loudspeaker, positionned either at the right or at the left of the MEMS array (see Fig. 5 at left). The loudspeaker is driven by a white noise generator whose spectrum is plotted in Fig. 5 at right. The

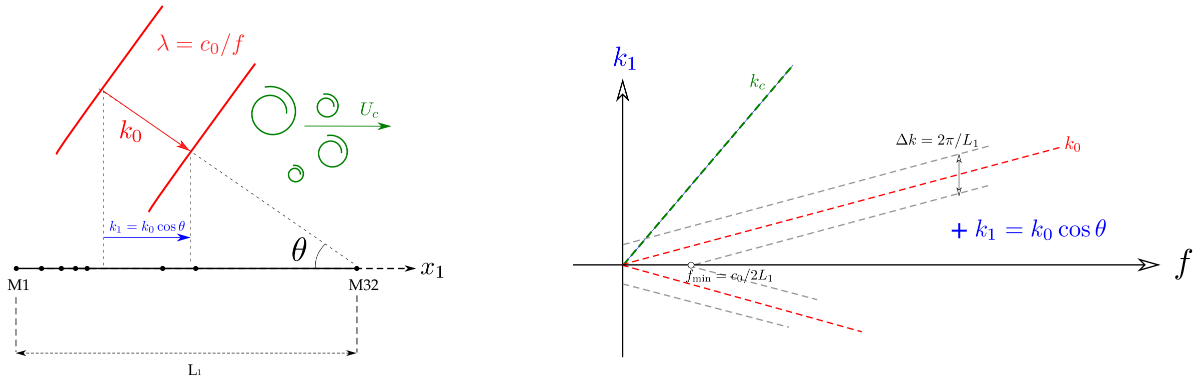

Fig. 4 Sketch of the wavenumber analysis. At left : acoustic wave impacting the MEMS array, with an angle θ, below a turbulence field convected at U_c. At right : scheme of the one-dimensionnal wavenumber spectrum, with the acoustic and the hydrodynamic contributions.

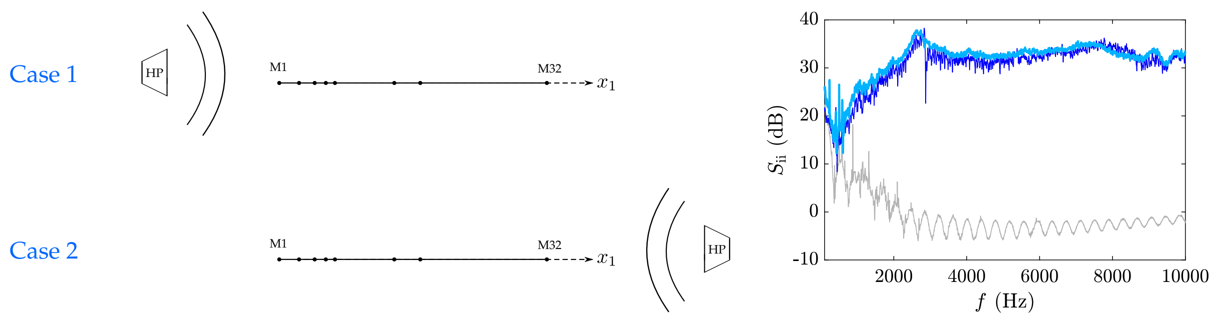

Fig. 5 Acoustic test case of the new MEMS array. At left : sketch of the experiment. At right : Spectrum of the central microphone of the antenna, under a white noise excitation. ——— : Obtained using the Welch method. ——— : Filtered spectrum, obtained through the integration of the low-wavenumbers components. ——— : Background noise during the experiment.

experiment enables a correct excitation up to 10 kHz. The lower levels observed below 2 kHz are due to the frequency response of the loudspeaker.

The one-dimensionnal wavenumber spectra are plotted in Fig. 6. On this figure, the acoustic wavenumber $k_0 = \pm 2\pi f/c_0$ is plotted using dashed lines. These wavenumber transforms exhibit acoustic waves propagating either from the left to the right (case 1, see Fig. 6 at left) or from the right to the left (case 2, see Fig. 6 at right). This test also enables the verification of the wavenumber resolution of the MEMS array, which is $\Delta k = 2\pi/L_1 = 18$ rad/m. In other words, if the frequency is lower than $f_{\min} = c_0/(2L_1) = 490$ Hz, two acoustic contributions may not be separated in the wavenumber representation (also see Fig. 4).

At last, the integration of the acoustic contribution (see section III.A) is performed for each frequency. The resulting *filtered spectrum* is plotted in Fig. 5. Compared to the initial spectrum from Fig. 5 at right, this filtered spectrum exhibits a good agreement within 0.5 dB. Indeed, no flow is present, and the only contribution to the pressure field is the acoustic pressure.

C. Hydrodynamic test case

This academic configucation is conducted in the main subsonic wind tunnel of the Centre Acoustique at Ecole Centrale de Lyon in France. The flow is generated by a 800 kW two-stage centrifugal blower, delivering a nominal mass flow rate of 20 kg.s^{-1} up to Mach 0.5, in a 30×40 cm^2 section. Air passes through a settling chamber including a honeycomb and several wire meshes designed to reduce free stream turbulence. The acoustic treatement on the wind tunnel walls and baffled silencers allows noise reduction, and prevents acoustic contamination in the measurement zone. This results in an air flow at ambient temperature with a low background noise and a residual turbulence intensity

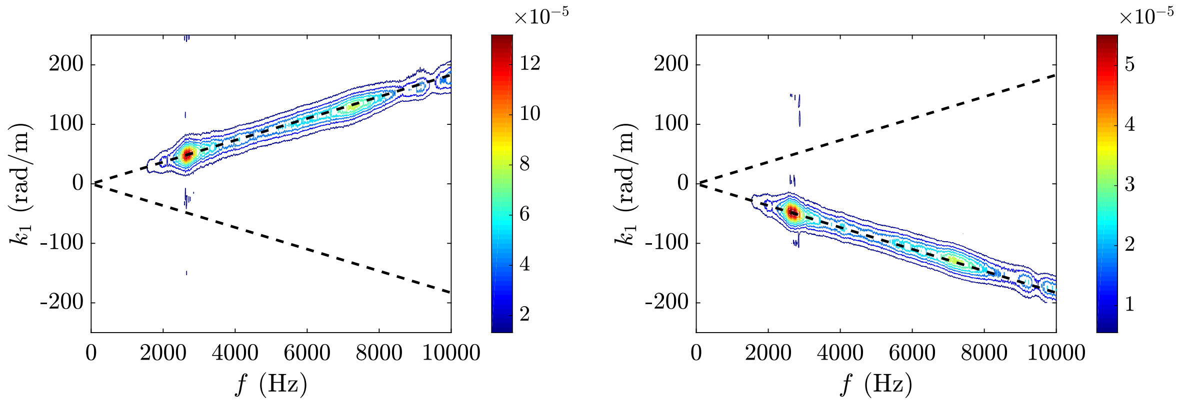

Fig. 6 One-dimensionnal wavenumber spectra with a white noise excitation, in Pa^2/Hz/m^{-1}. At left : acoustic wave propagating towards $x_1 > 0$ (case 1) ; at right : acoustic wave propagating towards $x_1 < 0$ (case 2).

smaller than 1%. Wall-pressure measurements are performed in the closed-section wind tunnel (see Fig. 7 at left), beneath a turbulent boundary-layer up to 50 m.s^{-1}.

Fig. 7 At left : Closed wind tunnel at Centre Acoustique, École Centrale de Lyon. At right : MEMS array with digital microphones, stuck onto the wind tunnel surface.

Hot-wire measurements were conducted to ensure the quality of the air flow and to extract the parameters of the boundary layer. Those parameters are indicated in figure 8 at left. The velocity profiles are plotted in figure 8 at right. The new MEMS array is positionned on the surface using a flat flare (see Fig. 7 at right). The flat flare is obtained using additive fabrication, and stuck onto the wind tunnel surface. Once installed and stuck, the whole MEMS array represents an excess thickness of 2.5 mm (see Fig 7 at right). It was checked using hot-wire anemometry that this small excess thickness does not change the velocity profiles significantly.

The one-dimensionnal spectra are plotted in Fig. 9 for increasing flow speed from 20 to 50 m/s. The convective ridge, due to wall-bounded turbulence (see Fig. 4), is clearly visible at the convective wavenumber k_c. This representation allows the extraction of the convection speed, which is around 80% of the free-stream velocity in this test case. Note that no acoustic contribution is visible in the wavenumber spectra. This is due to the new closed wind tunnel at Centre Acoustique, École Centrale de Lyon, which was designed to offer the lowest background noise possible.

U_∞	$\delta_1 \times 10^3$	H	u_τ	δ_{99}	Re$^+$
20.6	4.2	1.35	0.80	34.1	1760
31.9	4.1	1.32	1.19	40.2	3080
42.1	3.8	1.32	1.53	34.2	3360
51.8	3.6	1.32	1.88	29.0	3320

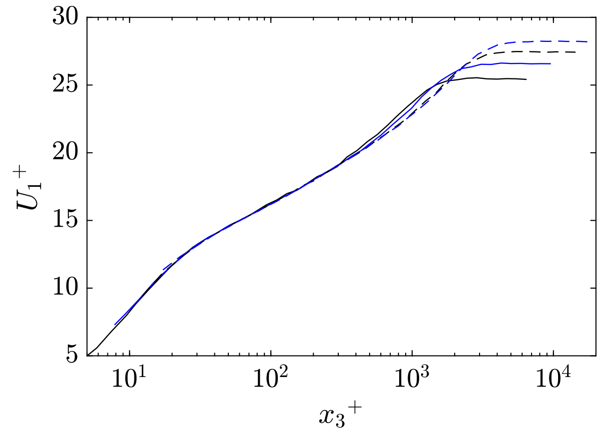

Fig. 8 At left : boundary layer parameters, extracted from the velocity profiles. At right : velocity profiles, in wall units, measured at —— : 20 m.s^{-1}, —— : 30 m.s^{-1}, - - - : 40 m.s^{-1}, - - - : 50 m.s^{-1}

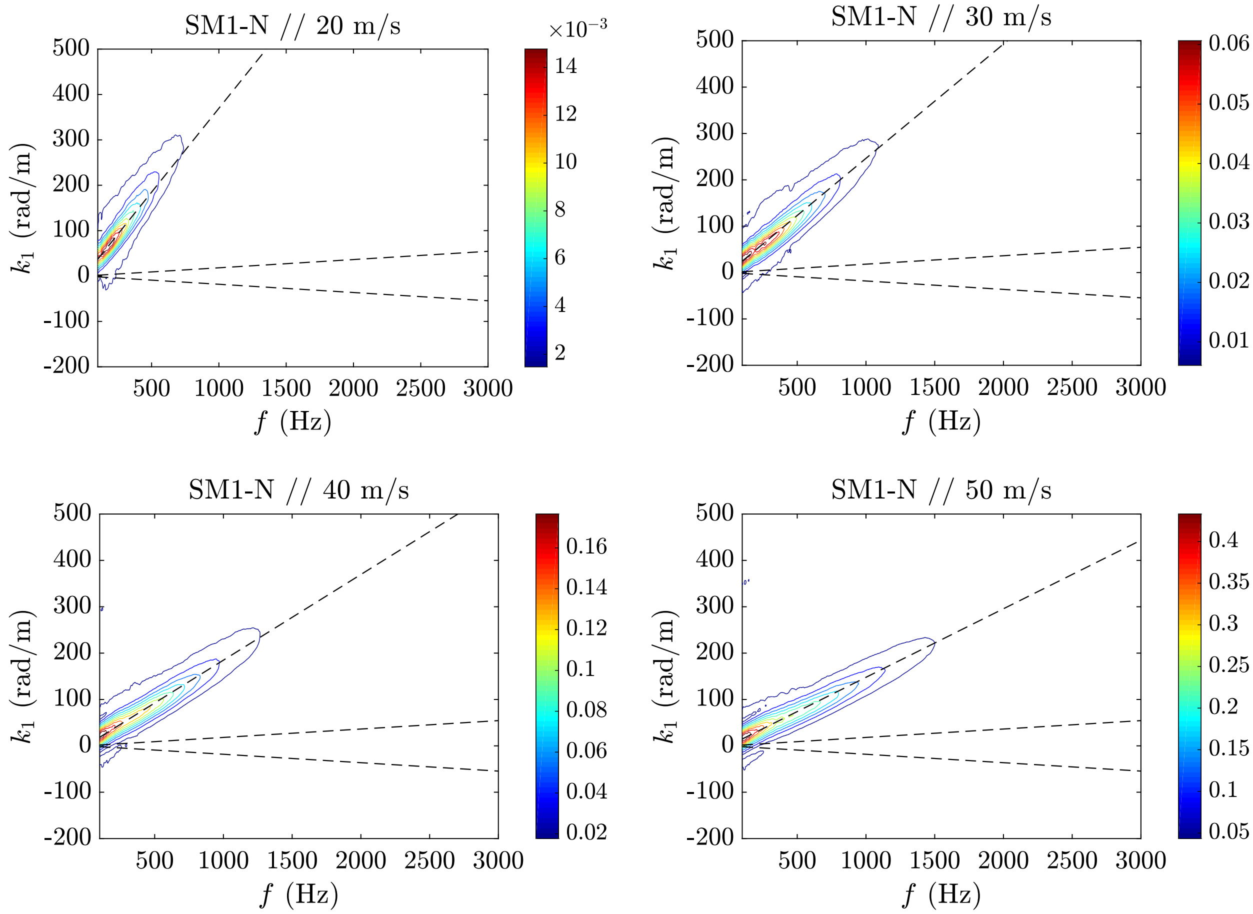

Fig. 9 One dimensionnal wavenumber spectra obtained at 20, 30, 40 and 50 m/s, in Pa^2/Hz/m^{-1}. The hydrodynamic and the acoustic wavenumbers are plotted as dashed lines (also see Fig. 4).

IV. Application: modal analysis of a ducted low-Mach number stage

A. Experimental set-up

The experiments are conducted in the low-Mach number ducted turbofan LP3 at Centre Acoustique, École Centrale de Lyon (see Fig. 10). This test-rig represents a 1:10 scaled fan of a turbofan engine. The test-rig is equipped with a Turbulence Control Screen (see Fig. 10 at left) and an anechoic termination downstream of the fan stage.

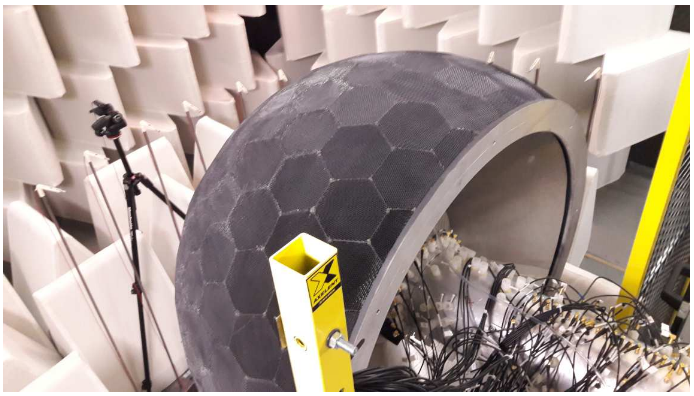

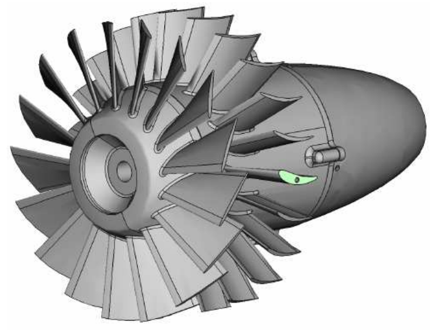

(a) Rotor-stator geometery.

Fig. 10 LP3 test-rig at Centre Acoustique, École Centrale de Lyon.

The rotation speed is imposed between 2000 and 10000 rpm. At fixed rotation speed, the mass-flow rate can be adjusted using a throttle system. The operating points of the test-rig are plotted in Fig. 11 at right. Amongst those operating points, the present study focuses on the points indicated in table 1.

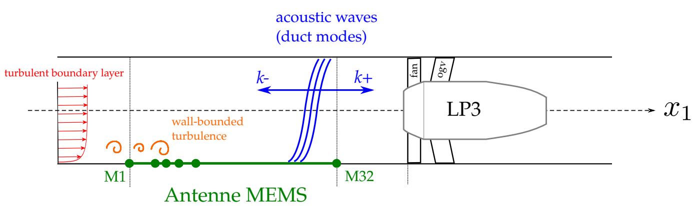

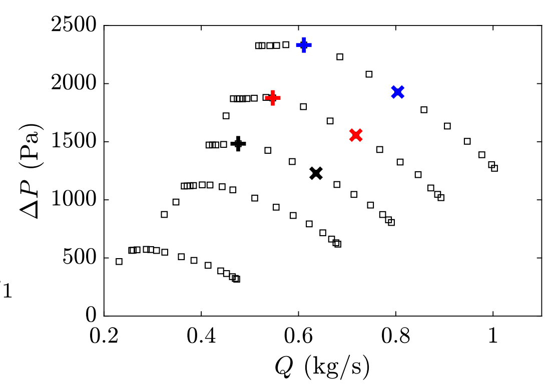

Fig. 11 At left : sketch of the experiment. At right : Operating points of the LP3 test rig, for rotation speeds of 5000 rpm, 7000 rpm, 8000 rpm, 9000 rpm and 10000 rpm.

The digital MEMS array is flush-mounted inside the LP3 test-rig duct using a 3D-printed support. The MEMS array is oriented in the streamwise direction: the microphone n^{o}1 facing the inlet, and the microphone n^{o}32 facing the LP3 stage (see Fig. 11 at left).

B. Results

1. *Pressure spectra*

Spectra are plotted in figure 12 for increasing rotation speeds of 8000, 9000 and 10000 tr/min respectively. The shapes of the spectra are coherent with previous studies on the same test-bench with a different instrumentation [12].

N (tr/min)	Q (kg/s)	U_d (m/s)	ΔP (Pa)	U_c (m/s)	U_c/U_d	
8000	0.64	23.5	1230	20	0.85	×
8000	0.48	17.6	1480	15	0.85	+
9000	0.72	26.4	1560	23	0.87	×
9000	0.55	20.2	1880	18	0.89	+
10000	0.80	29.4	1930	25	0.85	×
10000	0.61	22.4	2330	20	0.89	+

Table 1 Operating points of interest in the present study.

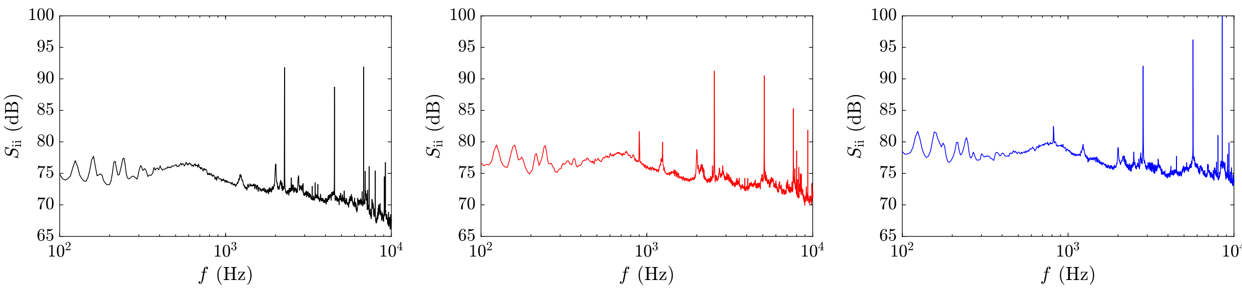

Fig. 12 Wall-pressure spectra for increasing rotationnal speeds: —— : 8 000 rpm, —— : 9 000 rpm and —— : 10 000 rpm.

2. Wavenumber analysis

In this section, the analysis takes advantage of the wavenumber representation described in III.A. The one-dimensionnal wavenumber spectra are plotted in Fig. 13. Two major contributions can be highlighted.

The first contribution is due to the wall-bounded turbulence, located around the convection wavenumber $k_c = \omega/U_c$. The detection of the peak of the convective ridge enables the measurement of the convection velocity U_c. The result is reported in table 1, and plotted as dashed lines in Fig. 13. This method indicates that the convection velocity is between 85 to 89% of the free-stream velocity (see Table 1).

The second contribution, clearly visible for all operating points from figure 13, is due to acoustic waves propagating in the duct. In the wavenumber representation, this contribution is visible if the wavenumber is smaller than $k_0 = \pm\omega/c_0$. This contribution is mainly visible in the negative wavenumbers. This indicates acoustic waves propagating upstream in the duct – from the rotor / stator stage towards the test rig inlet –. Inside the acoustic region, some *spots* are clearly identified. This indicates that the acoustic field differs from a diffuse sound fields, and rather exhibits modal features. Those modal features are analysed in the next section.

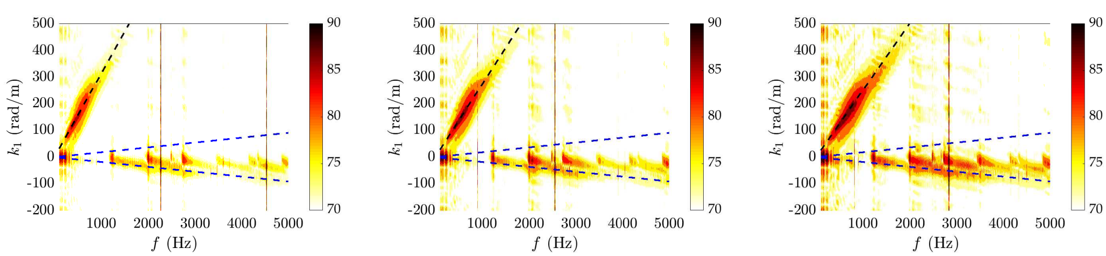

Fig. 13 Wavenumber spectra obtained at 8 000 rmp (left), 9 000 rpm (center) and 10 000 rpm (right), in dB (ref 2×10^{-5} Pa). - - - : acoustic wavenumber $k_0 = \pm\omega/c_0$. - - - : convective wavenumber $k_c = \omega/U_c$.

As described in III.A, a spatial filtering is possible to extract a specific component of the wavenumber representation. The *acoustic spectrum* is extracted, frequency by frequency, by integrating all the acoustic contributions from both propagation directions. The result at 10 000 rpm obtained from the wavenumber spectrum of figure 13 at right is plotted in figure 14. The initial spectrum (see Fig. 12 at right), obtained through the Welch method, is also plotted for comparison. The acoustic spectrum (in grey) is around 10 to 15 dB lower than the wall-pressure spectrum, depending on the frequency. This difference is attributed to the filtering of the wall-bounded turbulence contribution to the wall-pressure spectra – the denoising of the wall-pressure spectra –. Furthermore, thanks to this filtering, the frequency bumps due to the frequency cut-off of the duct modes are now clearly visible. We also observe a difference of around 10 dB between the upstream and downstream propagating waves. This effect is due to the anechoic termination of the test-rig, located downstream of the fan stage.

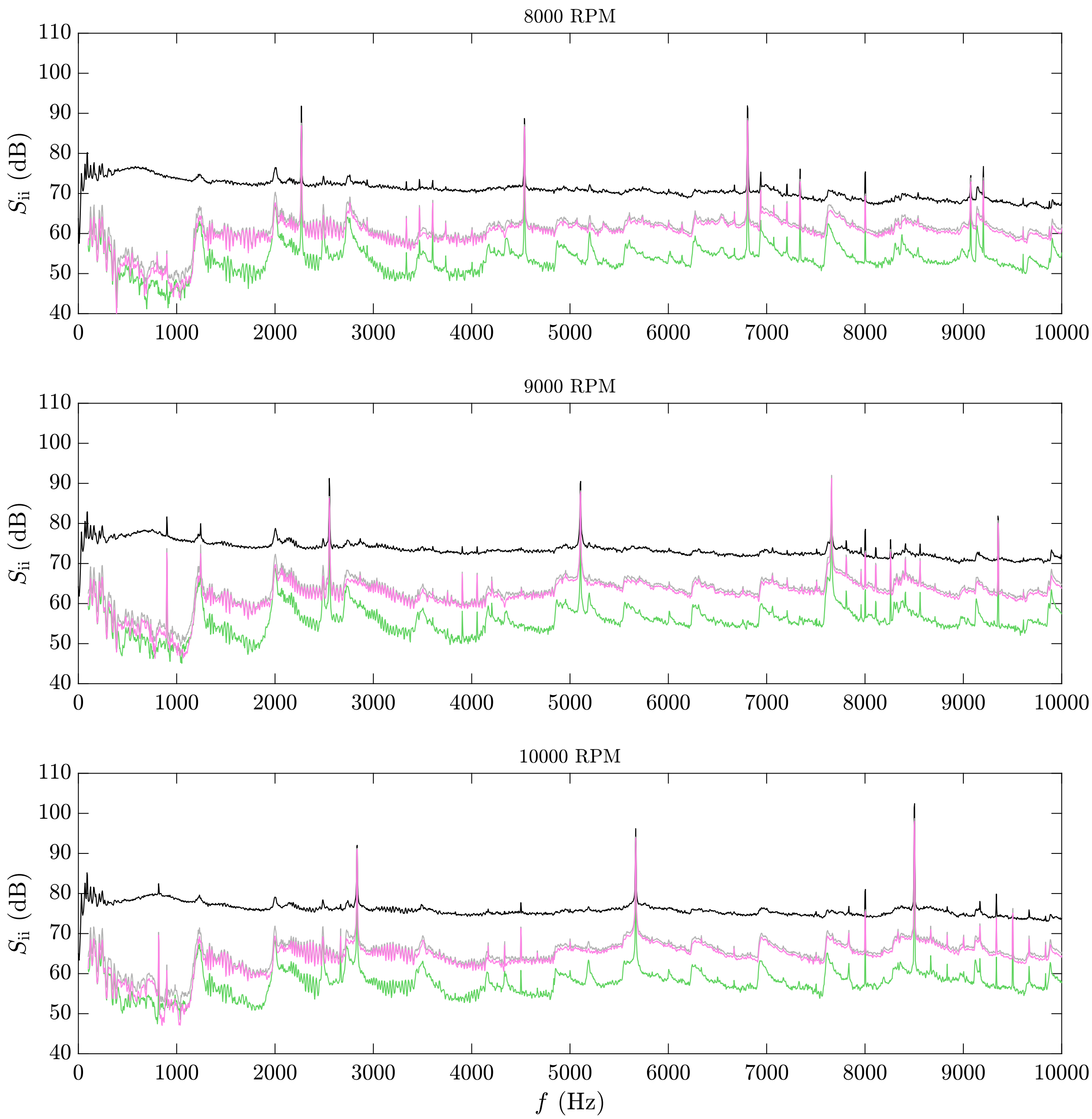

Fig. 14 Spectra obtained for increasing rotationnal speeds. —— : Wall-pressure spectrum, —— : acoustic spectrum (integrated over the acoustic wavenumbers), —— upstream propagating waves, —— downstream propagating waves.

3. Modal analysis using the wavenumber representation

In the case of a cylindrical duct with rigid walls, the frequency cut-off of a mode (m, n) is given by [15] :

$$f_{mn}^{(c)} = \frac{\lambda_{mn} c_0}{2\pi R} \tag{2}$$

where R is the duct radius, and c_0 the speed of sound. The eigenvalue λ_{mn} is obtained through the annulation of the derivative of the Bessel function, through [3]:

$$J'_m(\lambda_{mn}) = 0$$

In the wavenumber representation, a pressure mode propagating with an angle ϕ_{mn} will produce, in the array direction, a projected wavenumber (see Fig. 4):

$$k_{mn} = k_0 \cos(\phi_{mn}) \tag{3}$$

where $k_0 = \pm\omega/(c_0 \pm U_0)$ is the acoustic wavenumber in the presence of flow. The orientation of a particular mode (m, n) is linked to its eigenvalue λ_{mn} as in Eq. 4, where the $\overline{\cdot}$ notation denotes the Prandtl-Glauert transformation [9, 15]:

$$\sin(\overline{\phi_{mn}}) = \frac{\lambda_{mn}}{k_0 \overline{R}} \tag{4}$$

with, in the presence of flow defined by the Mach number M_0,

$$\sin(\phi_{mn}) = \frac{\sin(\overline{\phi_{mn}})}{\sqrt{1 - {M_0}^2 \cos(\overline{\phi_{mn}})^2}} \quad , \quad \overline{R} = \frac{R}{\beta} \quad \text{and} \quad \beta = \sqrt{1 - M_0^2}$$

In figure 15, interest is focused on the acoustic region from the one-dimensionnal wavenumber spectrum obtained at 10 000 rpm (see Fig. 13 on the right). On this figure, the orientation of the first 11 longitudinal modes has been reported as from Eq. 3. As the frequency increases, the emergence of high-order modes is clearly visible. Each cut-off frequency from Eq. 2 is associated with a spot in the wavenumber representation. This spot is first visible at $k_1 = 0$, because, close to its cut-off frequency, a particular mode has a propagation angle close to 90°. As the frequency increases, the propagation angle of a particular mode diminishes and tends to zero. The wavenumber associated to this particular mode tends to the acoustic wavenumber $\pm\omega/(c_0 \pm U_0)$. Furthermore, this evolution operates towards the negative wavenumbers as the modes mainly propagate upstream.

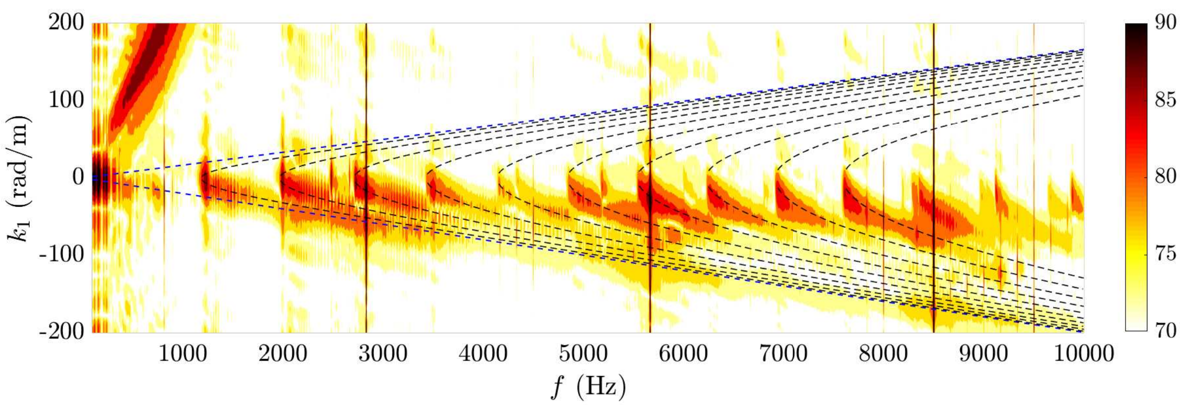

Fig. 15 Wavenumber - frequency spectrum, obtained at 10 000 rpm (same as Fig. 13 on the right), in dB (ref 2×10^{-5} Pa). The orientations of the wavevectors of the first 11 higher order modes are indicated as dashed lines.

V. Conclusion

In this study, a new high-resolution microphone array, using digital microphones, is introduced. This array is designed and tested under well-controlled acoustic and aerodynamic excitations. The array geometry is optimized to minimize the spatial aliasing, thanks to a non-uniform spacing with unique distances between every pairs of microphones of the array. A wavenumber approach is then used to explicitely extract the acoustic contribution of a low-Mach number stage and the hydrodynamic features of the wall-pressure fluctuations. Following previous studies by some of the present authors [2, 16], the feasibility of extracting the acoustic contribution, from a wall-pressure signal beneath a grazing flow, is demonstrated. Starting from the extracted acoustic contribution, a modal analysis is conducted using the wavenumber representation and the modal features of the low-Mach number stage are recovered. In the future, the LP3 test-rig will be equipped with several arrays, including microphone rings. Radial and azimuthal modal analysis will then be performed on different configurations, including the comparison between homogeneous and heterogeneous stators.

Acknowledgments

This work was performed within the framework of the Labex CeLyA of the Université de Lyon, within the programme "Investissements d'Avenir" (ANR-10-LABX-0060/ANR-16-IDEX-0005) operated by the French National Research Agency (ANR). Financial support by the industrial Chair ADOPSYS, co-financed by Safran Aircraft Engines and the French National Research Agency ANR (ANR-13-CHIN-0001-01), is also acknowledged. The authors are particularly grateful to Pascal Souchotte for his help in setting up the experiment.

References

[1] Abraham, B. M. & Keith W. L., 1998, Direct measurements of turbulent boundary layer wall pressure wavenumber-frequency spectra, *J. Fluid Eng.*, **120**, 29-39.

[2] Arguillat, B., Ricot, D., Bailly, C. & Robert, G., 2010, Measured wavenumber - frequency spectrum associated with acoustic and aerodynamic wall pressure fluctuations, *J. Acoust. Soc. Am.*, **128**(4), 1647-1655.

[3] Bennett, G. J., O'Reilly, C., Tapken, U. & Fitzpatrick, J., 2009, Noise source location in turbomachinery using coherence based modal decomposition, 15th AIAA/CEAS Aeroacoustics Conference, AIAA Paper 2009-3367.

[4] Blake, W.K., 1986, Essentials of turbulent wall-pressure fluctuations, in Mechanics of flow-induced sound and vibration, Vol. II Complex flow-structure interactions, *Academic Press Inc.*, Orlando, Florida.

[5] Bremner, P., Todter, C. & Clifton, S., 2015, Sideglass turbulence and wind noise sources measured with a high resolution surface pressure array, *SAE Int. J. Passeng. Car - Mech. Syst.*, **8**(3), 1063–1074.

[6] Bull, M.K., 1996, Wall-pressure fluctuations beneath turbulent boundary layers: some reflections on forty years of research, *J. Sound Vib.*, **190**(3), 299–315.

[7] Corcos, G. M., 1964, The structure of the turbulent pressure field in boundary-layer flows, *J. Fluid Mech.*, **18**(3), 353–378.

[8] Finez, A., Pereira, A., & Leclere, Q., 2015, Broadband mode decomposition of ducted fan noise using cross-spectral matrix denoising, FAN2015 Conference, 15-17 April 2015, Lyon, France.

[9] Lowis, C.R., Joseph, P.F. and Kempton, A.J., 2010, Estimation of the far-field directivity of broadband aeroengine fan noise using an in-duct axial microphone array, *J. Sound Vib.*, **329**, 3940-3957.

[10] Morfey, C. L., 1964, Rotating pressure patterns in ducts: their generation and transmission, *J. Sound Vib.*, **I**, 60-87.

[11] Neise, W. & Ulf, M., 1994, Aerodynamic noise of turbomachines, *DLR Internal Report*, 22314-94/B5.

[12] Pestana, M., Pereira, A., Salze, E., Thisse, J., Sanjosé, M., Jondeau, E., Souchotte, P., Roger, M., Moreau, S., Regnard, J. & Gruber, M., 2017, Aeroacoustics of an axial ducted low Mach-number stage: numerical and experimental investigation, 23rd AIAA/CEAS Aeroacoustics Conference, AIAA Paper 2017-3215.

[13] Prigent, S., Engleman, R. Salze, E. & Bailly, C., 2018, Deconvolution of the wave number - frequency spectra of wall pressure fluctuations, 24th AIAA/CEAS Aeroacoustics Conference, AIAA Paper 2018-3291.

[14] Rice, E. J., Heidmann, M. F. & Sofrin, T. G., 1979, Modal propagation angles in a cylindrical duct with flow and their relation to sound radiation, 17th Aerospace sciences meeting, January 15-17, paper 79-0183.

[15] Rienstra, S. W., 2015, Fondamentals of Duct Acoustics, *VKI Lecture Series*.

[16] Salze, E., Bailly, C., Marsden, O., Jondeau, E. and Juvé, D., 2014, An experimental characterization of wall pressure wavenumber-frequency spectra in the presence of pressure gradients, 20th AIAA/CEAS Aeroacoustics Conference, AIAA Paper 2014-2909.

[17] Tapken U., Raitor, T. & Enghardt, L., 2009, Tonal noise radiation from an UHBR fan-optimized in-duct radial mode analysis, 15th AIAA/CEAS Aeroacoustics Conference, AIAA Paper 2009-3288.

[18] Tyler, J. M. & Sofrin, T. G., 1961, Axial flow compressor noise studies, SAE Technical Paper 620532.